Int. J. Electrochem. Sci., 13 **(2018)** 719 – 738, doi: 10.20964/2018.01.92

International Journal of
ELECTROCHEMICAL
SCIENCE
www.electrochemsci.org

Continuous Monitoring of Steel Corrosion Condition in Concrete Under Drying/Wetting Exposure to Chloride Solution by Embedded MnO_2 Sensor

Ming Jin[1], *Song Gao*[1], *Linhua Jiang*[1,2,3,*], *Yu Jiang*[4], *Dan Wu*[1] , *Ruitong Song*[1], *Yirui Wu*[1], *Junqiao He*[1],

[1] College of Mechanics and Materials, Hohai University, Nanjing 210098, PR China
[2] National Engineering Research Center of Water Resources Efficient Utilization and Engineering Safety, Nanjing 210098, PR China
[3] Engineering Research Center on New Materials and Protection in Hydraulic, Jiangsu Province, 1 Xikang Rd., Nanjing 210098, PR China
[4] Department of Civil & Environmental Engineering, Washington State University, Pullman, WA 99164, USA
[*]E-mail: hhulhjiang@gmail.com, jinming@hhu.edu.cn

Received: 7 July 2017 / *Accepted:* 27 November 2017 / *Published:* 16 December 2017

Corrosion condition of steel in concrete under drying/wetting exposure to chloride ion solution was monitored based on various electrochemical techniques including linear polarization (LP), electrochemical impedance spectra (EIS) and half-cell potential (HCP) through embedded MnO_2 reference electrode. In LP measurement, polarization resistance of steel was equal to the slope of curves. However, in EIS measurement, polarization resistance of steel was calculated by adding the resistance of protective film to the charge transfer resistance derived from EIS data by means of the equilibrium circuit model. Corrosion state of steel was differentiated based on the obtained corrosion current density calculated by the polarization resistance according to the Stern-Geary equation by introducing the ″divergent region″. Furthermore, potential of steel with respect to embedded MnO_2 reference electrode was higher than -0.400 V, -0.400 to -0.516 V, -0.516 to -0.710 V and lower than -0.710 V for passive state, critical corrosion state, moderate corrosion rate state and high corrosion rate state respectively. Continuous non-destructive monitoring corrosion condition of steel in concrete was achieved through embedded MnO_2 reference electrode via electrochemical techniques.

Keywords: MnO_2, Reinforced Corrosion, Monitoring, Concrete, EIS, LP, HCP, Sensor

1. INTRODUCTION

Reinforced steel has been widely integrated in concrete structure in which rebar is protected by the formation of passive film in the high alkaline concrete environment. Nevertheless, corrosion of

steel is initiated once the passive film is damaged due to the aggressive mediums such as chloride ion and carbon dioxide. Corrosion propagation will lead to deterioration of structure that influences the safety as well as serviceability of concrete structure[1]. Therefore, the structure risk related to steel corrosion is promoting the application of embedded sensors to monitor and evaluate the condition of steel in concrete, which can remind the need for repair of structure before reaching dangerous levels of damage[2].

Since the reinforced steel corrosion is electrochemical in nature, electrochemical techniques are appropriate to measure the corrosion condition of steel in concrete structure, including half-cell potential (HCP) technique[3-5], linear polarization (LP) technique[6], electrochemical impedance spectroscopy (EIS) technique[7-9] and potentiodynamic polarization (PP) technique[10,11]. Even though the dynamic information concerning the steel condition can be measured by PP technique, the strong polarization potential interval applied to steel is up to hundreds even thousands of mV which causes significant damage on the steel surface therefore continuous monitoring of steel corrosion in concrete structure by PP technique is almost impossible[6]. Fortunately, sustainable continuous and evaluation of steel condition in concrete can be realized by means of the other three techniques.

Monitoring corrosion condition of steel in concrete by electrochemical techniques calls for a stable and rugged reference electrode (RE) which can be permanently embedded in concrete. Therefore, these interferences such as concrete cover and liquid junction potential on measurement results are reduced even eliminated. The liquid based saturated calomel electrode (SCE) and Ag/AgCl reference electrode are not suitable for embeddable use in concrete structures due to the leakage of internal liquid electrolyte[12]. Wei et al.[13] has placed a $Cu/CuSO_4$ RE into concrete to monitor the development of the steel corrosion in concrete under the alternated drying/wetting corrosion environment. However, this electrode usually exhibited poor stability and reliability in concrete environment. Duffo et al.[14] introduced the application of metal-metal oxide (MMO) activated titanium rod (ATR) as the reference electrode in concrete environment, nevertheless, the potential of this electrode was sensitive to pH value meanwhile it became less reproducible after placing in concrete over one year. In addition, the activated carbon electrode has been recommended by Abbas et al.[15]and He et al.[16] as the pseudo-reference for having the advantage of high electrical double layer capacitance, but Duffó et al.[17] reported the graphite pseudo-reference electrode was oxygen sensitive. In recent years the solid manganese dioxide (MnO_2) reference electrode has been proved to be most stable and reliable reference electrode in concrete environment[18,19]. Even though Karthick et al.[20] detected the states of steel in concrete incorporated by 0 and 3% NaCl by weight of cement representing the passive and active conditions of steel respectively through embedded MnO_2 RE, continuous evolution of steel in concrete exposed to chloride ion solution was not tested and verified. Meanwhile few studies have focused on sustainable monitoring of corrosion condition of steel in concrete by means of embeddable MnO_2 RE through different electrochemical techniques.

In this paper the evolution of corrosion condition of steel in concrete specimens under drying/wetting exposure to chloride solution was monitored by the embedded MnO_2 RE through various electrochemical techniques including LP, EIS and HCP. The determination of corrosion initiation of steel in concrete based on the obtained corrosion current density was also discussed.

2. EXPERIMENT

2.1 Materials

2.1.1 Cement

The cement was P.II 42.5 (GB175-2007) Ordinary Portland Cement (OPC) and its oxide composition has been indicated in Table 1.

Table 1. Chemical composition of OPC used in our work (%).

	SiO_2	Al_2O_3	CaO	Fe_2O_3	MgO	K_2O	Na_2O	SO_3	Ignition loss
OPC	22.55	9.35	61.30	3.10	1.35	1.03	0.15	0.99	0.16

2.1.2 Fine aggregate

The fine aggregate was the local clean river sand (fineness modulus of medium sand equal to 2.6). The specific gravity of fine aggregate was 2.5 and the water absorption of fine aggregate was 0.6%.

2.1.3 Coarse aggregate

Locally available well graded aggregate of size between 5 and 20 mm was used as coarse aggregates.

2.1.4 Carbon Steel

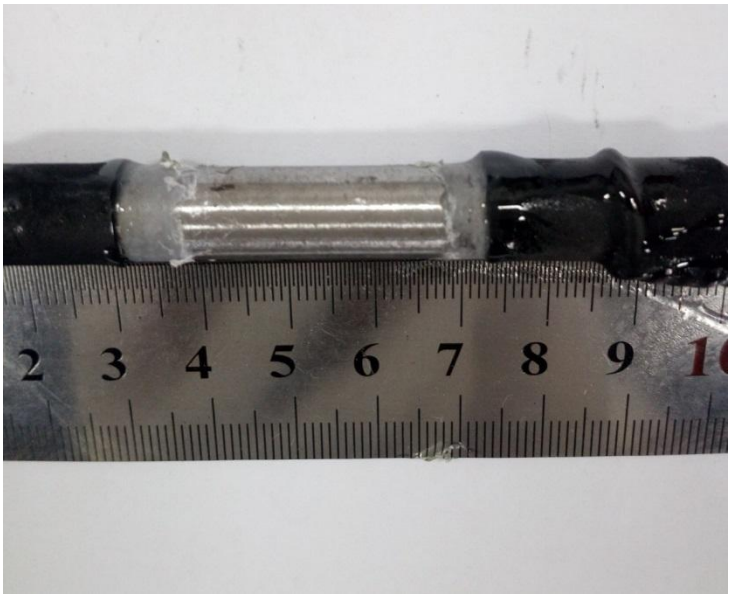

Figure 1. The photo of fabricated steel sample.

A cylindrical steel bar with a diameter of 1.0 cm and a length of 7.0 cm was used. The chemical composition (in wt%) was 0.22 C, 0.30 Si, 0.65 Mn, 0.05 S, 0.045 P and the residual Fe. In addition, the exposed length of the fabricated embedded steel was 3.0 cm therefore the exposed area was ca. 9.42 cm^2. The remaining part was sealed by hot-shrinkable tube. Fig. 1 shows the photo of prepared steel sample.

2.2 Fabrication of corrosion monitoring system

Embedded corrosion monitoring system assembly consists of a square stainless mesh electrode (ca. 9.00 cm^2) acting as counter electrode, MnO_2 electrode acting as reference electrode and carbon steel acting as working electrode. MnO_2 reference electrode includes three compartments namely a porous hydrated cement paste as bottom layer, a middle layer (i.e., the conductive alkaline slurry layer) as well as MnO_2 as the top layer.

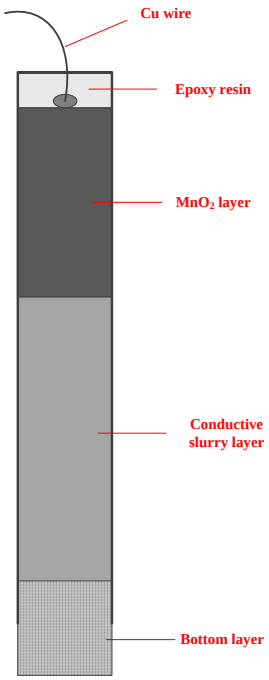

Figure 2. The scheme of fabricated MnO_2 reference electrode.

The water/cement ratio of cement paste applied in the bottom layer was 0.55 and the length of bottom layer was ca. 1.0 cm. Moreover, the middle layer was made up of $Ca(OH)_2$ gel which was fabricated by adding 1 g carboxymethyl hydroxyethyl cellulose in per 10 ml saturated $Ca(OH)_2$ solution. The length for this layer was ca. 3.0 cm. Finally, the top layer consisted of the MnO_2 powder which was firmly pressed with the compaction of approximately 2 psi and the length was ca. 2.0 cm. It should be noted that the diameter for every layer was 1.0 cm. A Cu wire was soldered with the MnO_2 layer meanwhile the top of the electrode was sealed with epoxy resin. The scheme of MnO_2 reference electrode is presented in Fig. 2.

2.3 Preparation of concrete specimens and corrosion test

Concrete specimens with the dimensions of 70×70×70 mm were cast. A designed mix of 1: 0.5: 1.5: 3.0 (cement: water: fine aggregate: coarse aggregate) was used. Each concrete specimen was assembled with a set of corrosion monitoring system. The scheme of the concrete specimen was shown in Fig. 3. It should be pointed out that the concrete cover depth was ca. 20 mm. After 24h, concrete specimens were demoulded and stored in a 95% humidity chamber at 20 ± 2 °C for 28 days of curing.

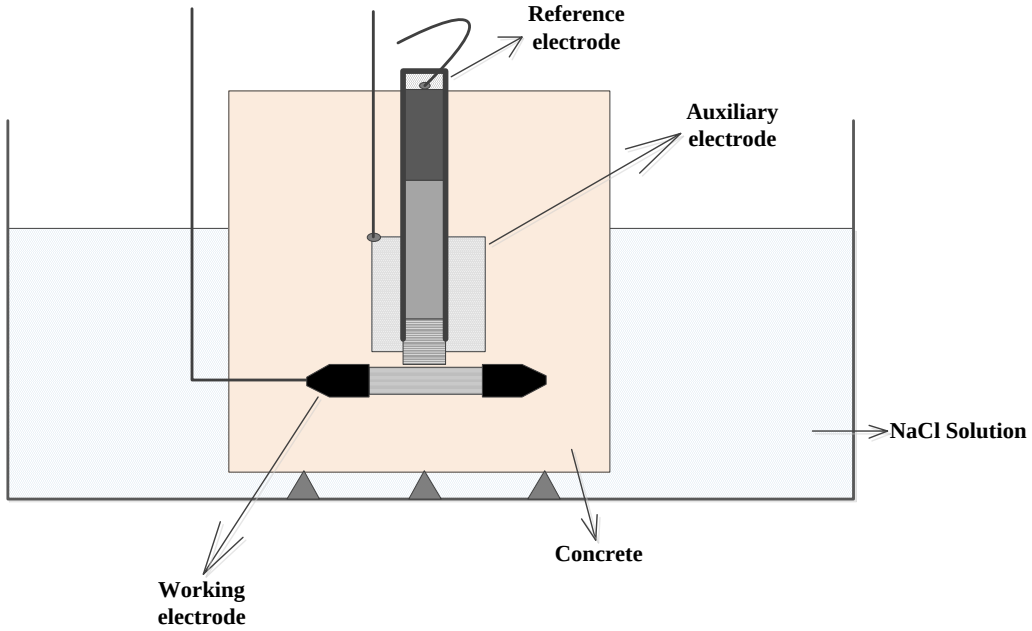

Figure 3. The scheme of concrete specimen with the embedded steel and corrosion monitoring system.

The accelerate corrosion test was performed by immersing concrete specimens in 3.5 wt % NaCl solution for 4 days, after that, an exposure for 3 days to temperature of 40°C was carried out. The cyclic period was one week. The total testing time was 12 weeks. To simplify the description, C1, C2, C3, C4, C8, C10 and C12 were used to refer to the 1st, 2nd, 3rd, 4th, 8th, 10th and 12th drying/wetting cycle, respectively.

2.4 Corrosion monitoring of steel by embedded monitoring system

All the electrochemical tests were performed with a Princeton Applied Research (PAR) STAT 2273 Potentiostat. If not specified, the tests were carried out at room temperature (25°C).

2.4.1 Linear polarization (LP) measurements

LP tests of steel was carried out after every drying/wetting (D/W) cycles, mainly during the wetting process of the cycles, by means of the embedded corrosion monitoring system with the scan procedure of -15 to +15 mV with respect to open circuit potential at a sweep rate of 0.166 mV/s.

2.4.2 Electrochemical impedance spectra (EIS) measurements

The same specimens used to experience LP measurements were also carried out with EIS tests which were performed at the open circuit potential with a 10 mV perturbation from 0.1 Hz to 100 KHz. These EIS data were analyzed using Zsimpwin software to obtain electrochemical parameters and related errors.

2.4.3 Half-cell potential (HCP) measurements

The HCP of steel was measured in every wetting process with respect to embedded MnO_2 RE.

2.4.4 Morphology observation

After 6 and 12 drying/wetting cycles, concrete specimens were split to observe the morphology of embedded steel. Furthermore, the micro-morphology of corrosion product was observed by field-emission scanning electron microscope (FE-SEM, Hitachi S4800).

3. RESULTS AND DISCUSSION

3.1 LP measurement of steel in concrete

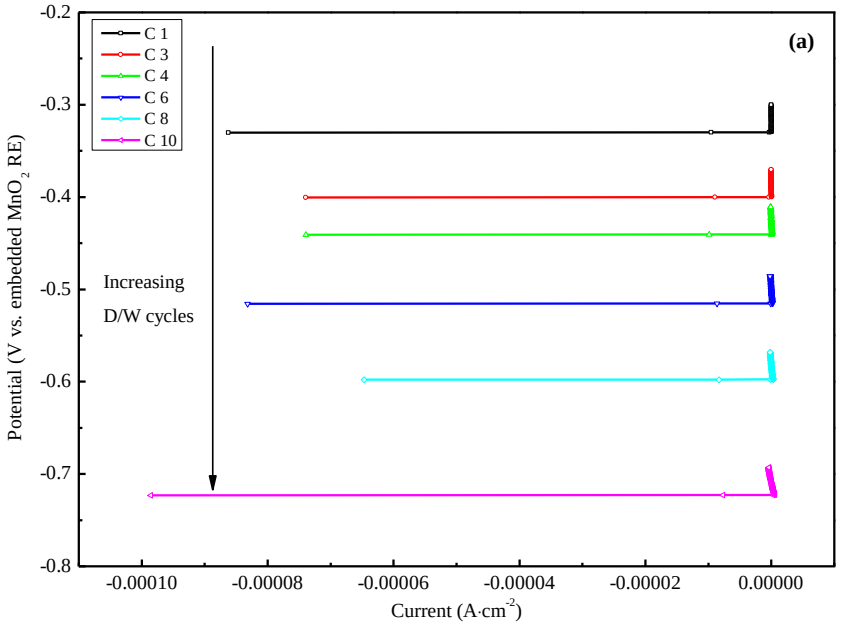

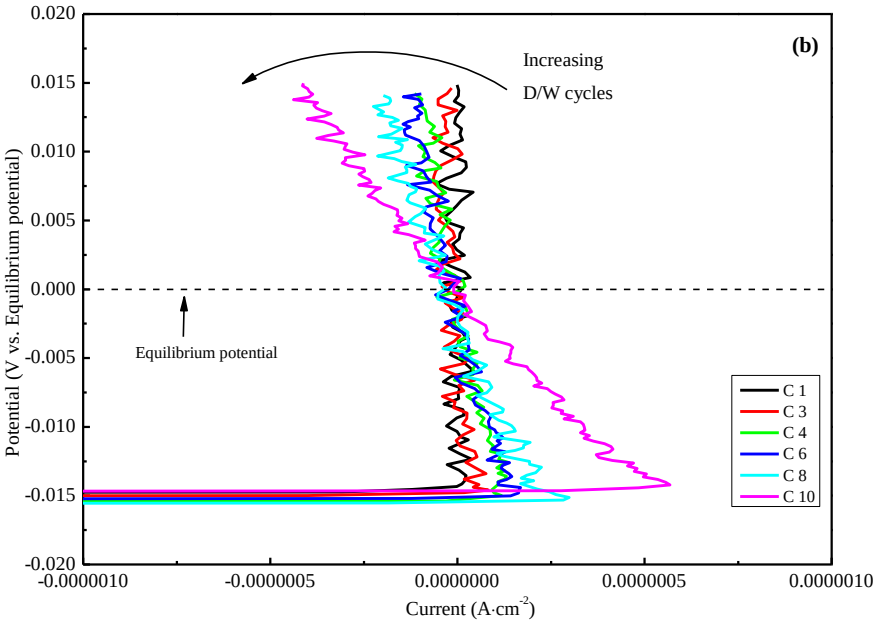

Figure 4. The evolution of LP curves of steel in concrete under drying/wetting cycle. (a) with respect to embedded MnO_2 RE, (b) with respect to the equilibrium potential.

Table 2. Polarization resistance of steel determined by LP technique in different D/W cycle.

D/W cycle(time)	1	2	3	4	5	6	7	8	9	10	11	12
Polarization resistance (kΩ)	394	138	78.9	53.1	37.8	30.3	14.8	10.2	7.77	6.00	3.52	2.82

Fig. 4 shows the evolution of typical LP curves of steel in concrete with the increasing drying/wetting (D/W) cycles. The linear response has been found out for relationships between steel potential and current during the whole LP measurements. The potential of steel exhibits a decreasing tendency with the increase of D/W cycle. However, the polarization resistance of steel is directly related to the slope of LP curve of steel. Fig. 4b presents the LP curves of steel with respect to the equilibrium potential in order to clearly display the development of slope of curve. Note that the equilibrium potential is equal to the value of open-circuit potential. Differing from the smooth lines in Fig. 4a, unsmooth lines have been found out for the LP curves in Fig. 4b due to the slight drift in the process of measurement even though the potential interval of LP technique applied to the steel was a weak polarization region, which can be attributed to the heterogeneous property of concrete structure. Besides, the shape of curve of steel changes from the near vertical line to the oblique line, indicating the slope of curve decreases with the increase of D/W cycle. The evolution of polarization resistance of steel determined based on the slope of LP curve in the D/W cycles process has been listed in Table 2. The chloride ion erosion in concrete changed steel from the passive condition to active one meanwhile the polarization resistance of steel was gradually decreased, meaning the anticorrosion ability of steel was weakened.

The corrosion current (I_{corr}) of steel in concrete was calculated based on the obtained polarization resistance according to the Stern-Geary equation, as presented in Eq. (1):

$$I_{corr}=\frac{B}{R_p} \qquad (1)$$

in which B is the Stern-Geary constant. A value of 26 mV has been adopted for active condition of steel and 52 mV for passive state, respectively[6]. R_p is the polarization resistance value of steel. Furthermore, the corrosion current density (i_{corr}) of steel was calculated through Eq. (2) in order to eliminate the influence of surface of steel on the results of corrosion information:

$$i_{corr}=\frac{I_{corr}}{A} \qquad (2)$$

where A is the area of active steel surface (ca. 9.42 cm^2). The accurate corrosion condition of steel in concrete is judged by the obtained corrosion current density, as described in literature[21]. In particular, steel is under passive condition in the case of i_{corr} value lower than 0.1 $\mu A \cdot cm^{-2}$ and in the moderate corrosion rate condition when the i_{corr} value reaches 0.5 $\mu A \cdot cm^{-2}$. Besides, steel is considered in the high corrosion rate state when the i_{corr} value exceeds $1\mu A \cdot cm^{-2}$. It makes significant senses to detect the depassivation state of steel in time through the corrosion current density. The evolution of corrosion current density of steel in concrete measured through the embedded MnO_2 RE has been indicated in Fig. 5.

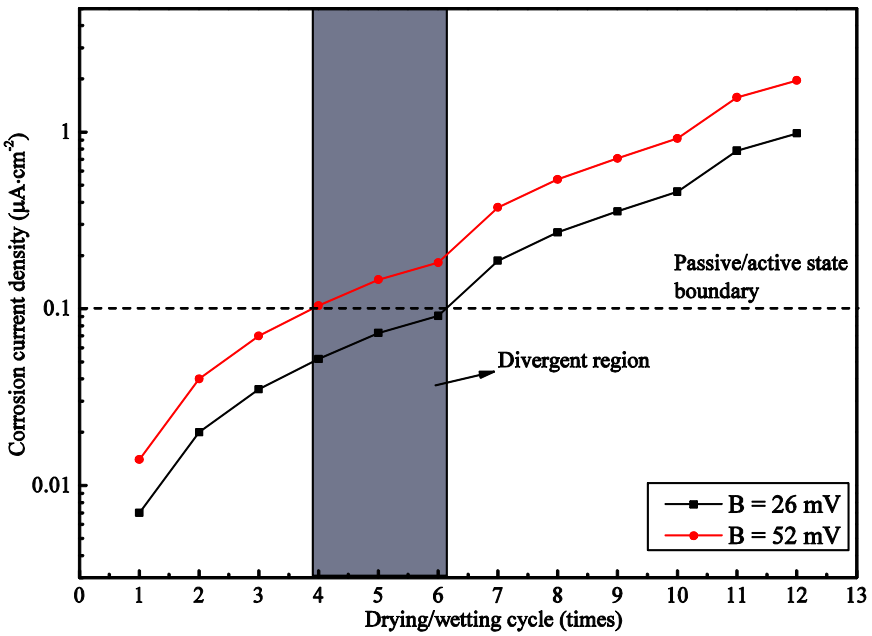

Figure 5. The evolution of corrosion current density of steel in concrete measured by LP technique through the embedded MnO_2 RE with the application of B values of 26 and 52 mV respectively.

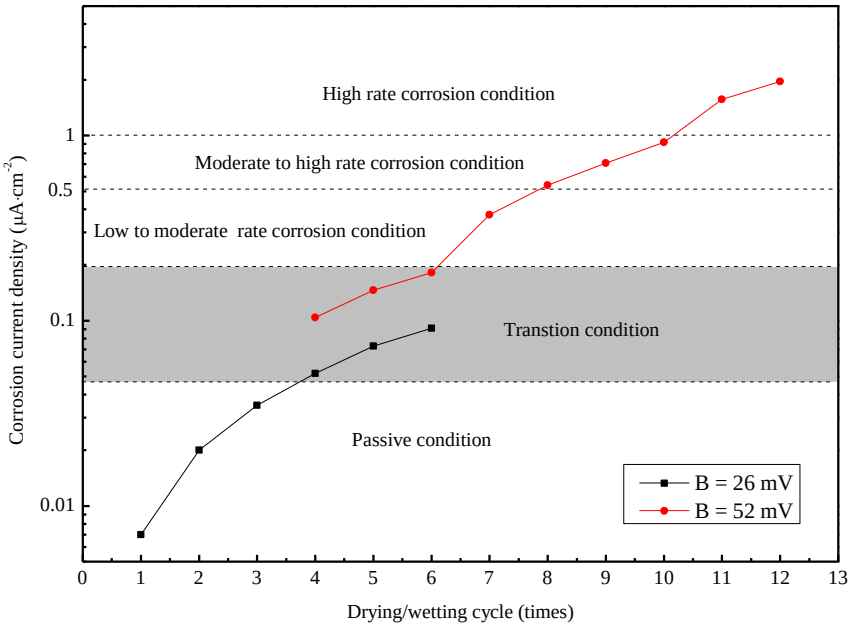

Figure 6. The evolution of steel state in concrete with the drying/wetting cycle determined based on LP technique.

In a word, the corrosion current density increases with the development of D/W cycles. Once the corrosion current density exceeds 0.1μA·cm^{-2} the steel is assessed in active condition. Before cycle 4, there is no controversy about the steel under the passive condition regardless of which *B* value is chosen. The steel state between cycle 4 and 6 is judged in passive condition in the situation of *B* value of 26 mV is chosen. On the contrary, steel is estimated under active condition when B value of 52 mV is applied. Therefore, there exists a ″divergent region″ on the evaluation of corrosion initiation of steel according to the Stern-Geary equation. Once the corrosion current density of steel enters this region, the steel should be considered in the transition condition which is between passive and active conditions. The polarization resistances by which the corrosion current density of steel calculated reaches 0.05 and 0.1μA·cm^{-2} respectively through the application of *B* value of 26 mV are regarded as the lower and upper limit values respectively of this ″divergent region″. Fig. 6 shows the evolution of steel states in the accelerated drying/wetting exposure to chloride solutions by introducing the transition condition. The steel at cycle 7 is found out to be low to moderate rate corrosion condition. Afterwards, steel is under moderate to high rate corrosion condition between cycle 8 and 10 and it reaches the high rate corrosion state after cycle 10. As described by Angst[22], definition of corrosion initiation of steel from the scientific point of view is recommended in determination of chloride ion threshold content. The transition condition presented in this work provides the characterization of corrosion initiation where the steel is considered in the critical condition of corrosion when the corrosion current density of steel enters the divergent region.

3.2 Electrochemical impedance spectra (EIS) measurement of steel in concrete

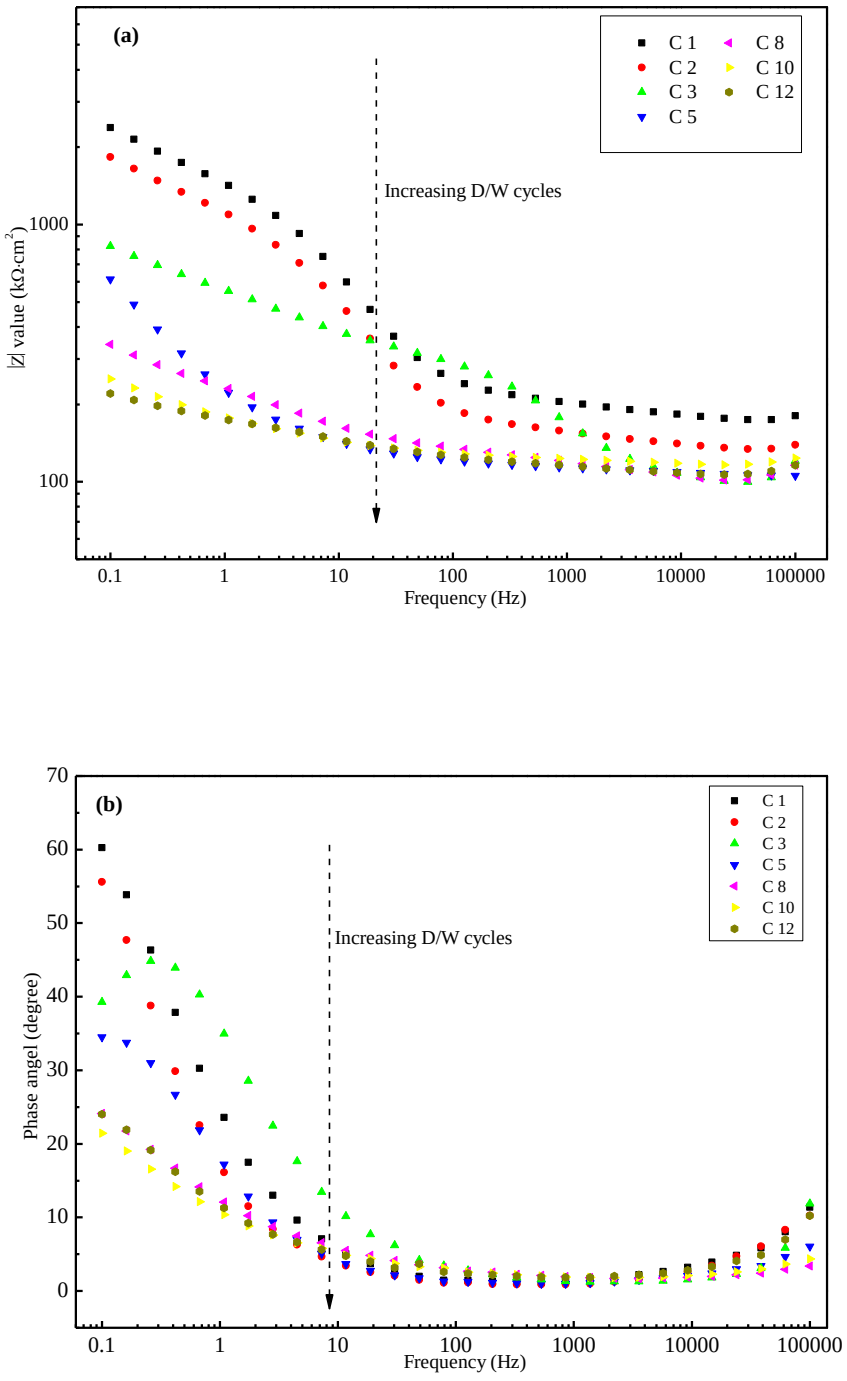

Figure 7. The development of Bode curves of steel in concrete with the drying/wetting cycle. (a) |z| plot, (b) phase angel plot.

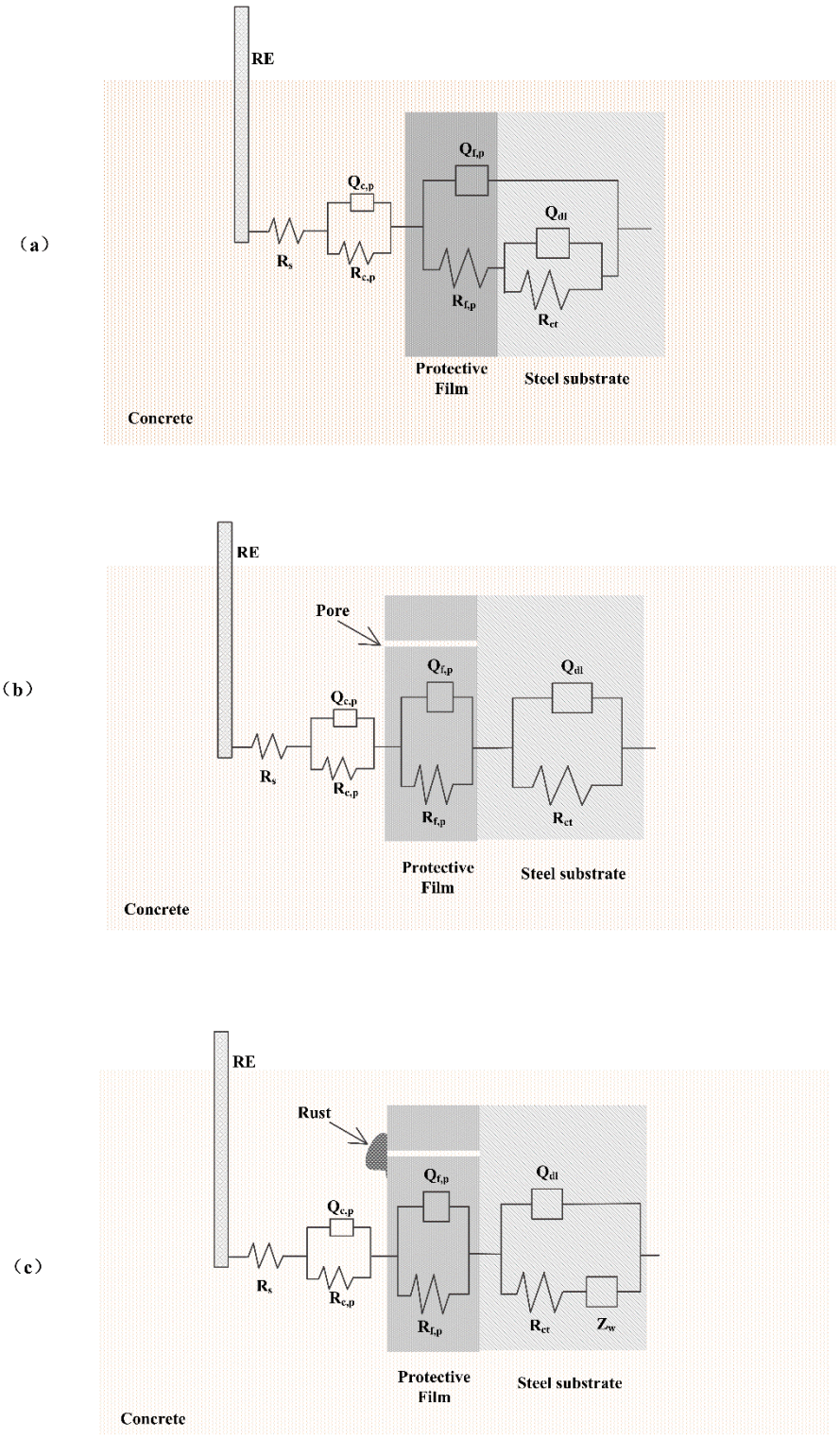

Figure 8. Physical models simulating the reinforced concrete system at different periods of accelerated corrosion tests and the corresponding ECM.

The evolution of Bode curves including $|z|$ plot and phase angel plot of steel in concrete measured by the EIS technique based on the embedded MnO_2 RE with the accelerated drying/wetting cycle is shown in Fig. 7. Generally speaking, the $|z|$ values of steel whether in high or low frequencies show the lowering tendency with the increase of D/W cycles. Significant decrease of $|z|$ value has been

observed after cycle 3. As for the phase angel curve, the peak value of phase angel presents at lowest frequency in the initial D/W cycles. The peak angel shifts towards larger frequency at cycle 3 meanwhile the lower value of peak angel has been observed compared to those measured in the initial cycles. However, the peak angel in the following phase angel curves returns back to the lowest frequency, which is different from the results reported by Wei[13]. In addition, the difference between the phase angel values after cycle 8 becomes negligible. These changes in Bode curves prove that complicated evolution processes and different dynamic features happen on the steel surface during the D/W cycles.

The equivalent-circuit model (ECM) was applied to analyze the EIS results in order to obtain the accurate information of steel conditions in different periods. Considering the surface roughness as well as the inhomogeneous spatial distribution of reaction on the steel surface, the constant phase element (CPE) is used instead of the pure capacitance to represent the capacitance, which is shown in the following:

$$Z_Q = \frac{1}{Y_o} \cdot (jw)^{-n} \qquad (3)$$

where Z_Q indicates the impedance of CPE, Y_o represents the admittance of CPE, w represents the angular frequency and n represents the dispersion power of CPE which is between 0 and 1. It should be pointed out that $n = 1$ represents an ideal capacitor. $j = (-1)^{1/2}$. Fig. 8 shows three physical models simulating the reinforced concrete system at different periods of accelerated corrosion tests and the corresponding ECM. In the ECM, R_s represents the contribution of the electrolyte resistance in concrete, the first time constant ($R_{c,p}$, $Q_{c,p}$) represents the property of pore network of concrete and the second time constant ($R_{f,p}$, $Q_{f,p}$) represents the redox process occurred on protective film on the steel surface, the third time constant (R_{ct}, Q_{dl}) represents the electrochemical reaction taking place on the steel substrate, the Z_w represents the Warburg resistance in the semi-infinite diffusion process.

The impedance of steel is high and the phase angel at low frequency reaches the peak at the initial cycle 1 and 2, meaning the steel under the passive condition therefore the reinforced concrete system in this stage is described by Fig. 8a. In the following stage (cycle 3 to 8), the total impedance value of steel deceases and the phase angel value drops at the low frequency, which indicates the locally destroyed protective film of steel and the resulting exposed steel substrate acts as the anode while the undamaged protective film acts as the cathode[23,24]. The corresponding model for reinforce concrete system in this stage is presented in Fig. 8b where the local corrosion happens on the steel surface and the charge transfer process plays the dominate role in the rate-controlled process of steel corrosion. Besides, the reinforced concrete system after cycle 8 is described by the application of Fig. 8c whose rate-controlled process includes charge transfer process as well as mass transfer process due to the accumulation of rust in the local damage region happened on the protective film. The obtained parameter values as well as the corresponding relative errors (E_{corr}) of EIS data for reinforce concrete system at different drying/wetting cycle are listed in Table 3.

Table 3. Fitting results of EIS data of steel by parallel equivalent circuit.

Cycle	R_s ($k\Omega \cdot cm^2$)	E_{corr} (%)	$Q_{c,p}$ ($\mu S \cdot S^{-n_{c,p}} \cdot cm^{-2}$)	E_{corr} (%)	$n_{c,p}$	E_{corr} (%)	$R_{c,p}$ ($k\Omega \cdot cm^2$)	E_{corr} (%)
1	180	35	3.41	25	0.35	27	13	38
2	139	41	3.71	37	0.37	25	17	31
3	125	27	3.12	29	0.40	22	25	35
5	105	31	2.81	23	0.42	27	38	27
8	119	28	2.31	25	0.41	20	49	32
10	134	26	1.89	18	0.45	23	55	26
12	146	35	1.57	22	0.44	21	61	30

Continued Table 3.

Cycle	$Q_{f,p}$ ($mS \cdot S^{-n_{f,p}} \cdot cm^{-2}$)	E_{corr} (%)	$n_{f,p}$	E_{corr} (%)	$R_{f,p}$ ($k\Omega \cdot cm^2$)	E_{corr} (%)	Q_{dl} ($mS \cdot S^{-n_{dl}} \cdot cm^{-2}$)	E_{corr} (%)
1	1.57	23	0.75	25	53	27	0.78	19
2	1.68	25	0.70	21	45	35	0.91	25
3	2.21	19	0.64	25	33	28	3.21	22
5	4.76	22	0.52	20	23	26	8.13	27
8	5.83	25	0.47	19	15	23	15	24
10	6.89	27	0.38	21	9.81	19	33	17
12	8.76	18	0.34	26	6.94	18	57	15

Continued Table 3.

Cycle	n_{dl}	E_{corr} (%)	R_{ct} ($k\Omega \cdot cm^2$)	E_{corr} (%)	Z_w ($S \cdot S^{-0.5} \cdot cm^{-2}$)	E_{corr} (%)
1	0.85	24	1947	30	-	-
2	0.81	19	793	35	-	-
3	0.73	21	476	35	-	-
5	0.64	17	269	28	-	-
8	0.57	23	51	23	-	-
10	0.49	16	27	31	8.75	22
12	0.42	21	15	27	15	26

The electrolyte resistance drops in the initial several cycles and then increases in the following cycles. The decrease of electrolyte resistance is attributed to the increase of chloride ion content in concrete pore solution due to the penetration of chloride ion into concrete. However, the increase of electrolyte resistance is related to the continuous hydration of cement paste in concrete, similar results have been presented by Polder[25]. The decrease of capacitance and increase of resistance related to

concrete pore network have been found out in the process of D/W cycle test. Besides, it is interesting to point out that the value of $n_{c,p}$ shows the increasing tendency with the D/W cycle, which is attributed to the sustained concrete compaction caused by the continuous hydration. Differing form the evolution of relevant features of concrete, the resistance of protective film as well as charge transfer resistance of steel decrease with the increasing D/W cycle. The charge transfer resistance of steel reduces from the initial thousands of $k\Omega \cdot cm^2$ to dozens of $k\Omega \cdot cm^2$ at the late drying/wetting experiment. Meanwhile, the resistance of protective film of steel shows the dozes of $k\Omega \cdot cm^2$ in the initial D/W cycles then it drops to several $k\Omega \cdot cm^2$ in the end of D/W cycle test. The decreases of resistance of protective film as well as charge transfer resistance indicate the increase of corrosive rate of steel due to the breakdown of protective film and initiation of corrosion[7,8]. In addition, the capacitances of protective film and steel substrate increase with the increasing D/W cycle and the higher value of capacitance for reinforced concrete interface is consistent with the lower resistance value[21,26]. Besides, the n values decrease in the accelerated D/W cycle because of the increase of roughness of steel surface produced by the damage of protective layer.

The polarization resistance of steel should be determined before obtaining the qualified information of corrosion rate. Taken consideration of the resistance of protective film on the steel surface, the polarization resistance (R_p) of steel is obtained by adding the resistance of protective film ($R_{f,p}$) to the charge transfer resistance (R_{ct}), as shown in Eq. (4):

$$R_p = R_{f,p} + R_{ct} \qquad (4)$$

Afterwards, the corrosion current density of steel is calculated based on the obtained polarization resistance through the combination of Eq. (1) and (2).

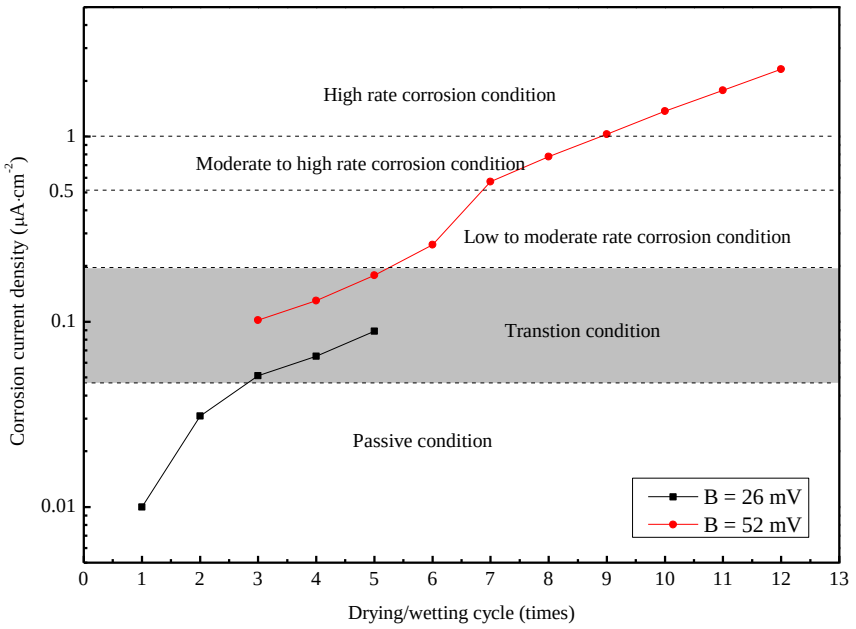

Figure 9. The evolution of corrosion current density and steel state in concrete with the drying/wetting cycle determined based on EIS technique.

Fig. 9 shows the evolutions of corrosion current density as well as steel state in the drying/wetting exposure to chloride solutions. The steel is located in the passive condition during the initial two D/W cycles and it entered the transition condition in the subsequent D/W cycle which continues until cycle 5. Then the steel was in the low to moderate rate corrosion condition at cycle 6 and in the moderate to high rate corrosion condition region from cycle 7 to 8. Finally the steel is under the high rate corrosion condition after cycle 9. In a word, the steel condition can be differentiated based on the corrosion current density obtained by EIS technique.

3.3 Half-cell potential measurements of steel

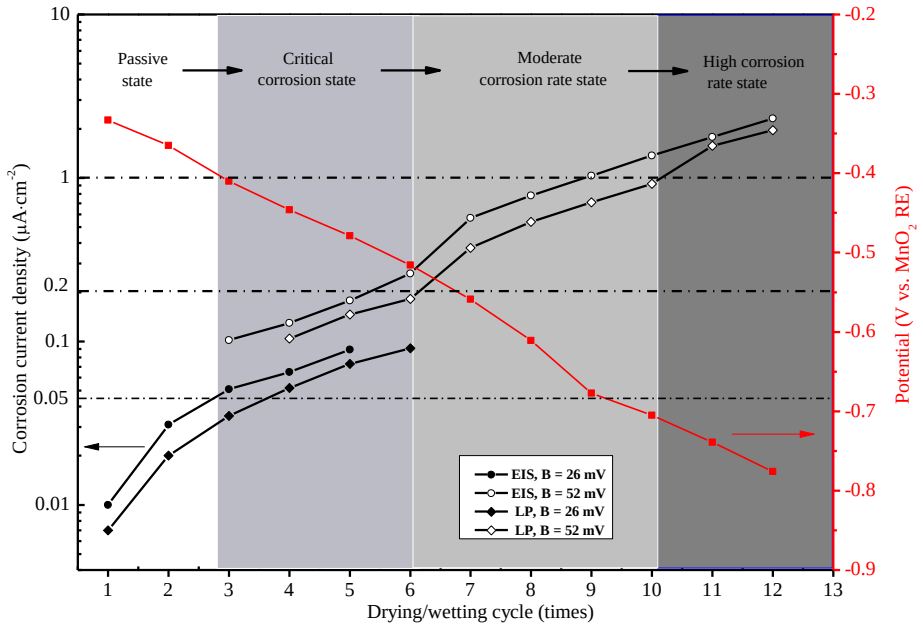

Figure 10. The evolution of half-cell potential (HCP) as well as steel state with the drying/wetting cycle.

Fig. 10 presents the evolution of half-cell potential (HCP) of steel as well as corrosion current densities obtained by LP and EIS techniques with the accelerated drying/wetting (D/W) cycle. The steel condition was divided into passive state, critical corrosion state, moderate corrosion rate state and high corrosion rate sate respectively based on the obtained corrosion current densities measured by EIS and LP techniques. Steel was considered in passive state when the potential was more positive than -0.400 V. The relevant mechanism describing the steel corrosion happened in the D/W experiment was explained by Fig. 11[27]. The anodic oxidation reaction occurred on the surface of steel was listed in Eq. (5):

$$Fe\text{-}2e^{-}\rightarrow Fe^{2+} \qquad (5)$$

However, the cathodic reduction reaction happened in the process of wetting was different from that in the process of drying. During the process of wetting, i.e., the humid circumstance, the

corrosion product ($Fe00H$) played a role of strong cathodic depolarization agent since that this product could adopt the electron released from anode. Hence, the cathodic reduction reaction was expressed by Eq. (6):

$$6Fe00H+2e^{-}\rightarrow 2Fe_3O_4+2H_2O+2OH^{-} \quad (6)$$

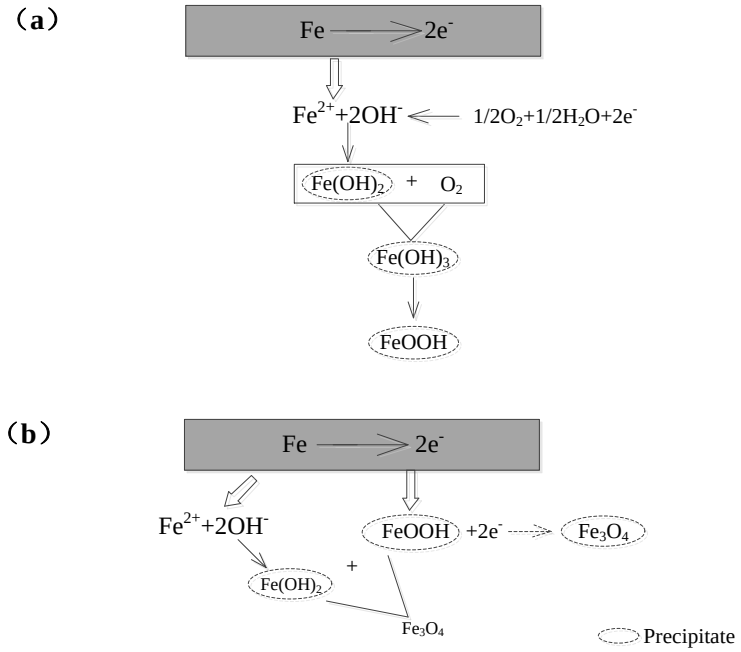

Figure 11. The scheme of mechanism describing the steel corrosion happened in the drying/wetting cycle.

Furthermore, continuous reaction between Fe^{2+} produced from anodic reaction and the corrosion product ($FeOOH$) was conducted to produce Fe_3O_4, which was explained by means of Eq. (7):

$$2FeOOH+Fe^{2+}+2OH^{-}\rightarrow Fe_3O_4+2H_2O \quad (7)$$

Actually, the reaction presented by Eq. (6) compensated the cathodic polarization due to the shortage of oxygen. The mass transfer resistance of Fe^{2+} hydration was reduced because of the continuous reduction of $FeOOH$ layer on the surface of steel. This resulted in higher content of Fe^{2+} dissolved into the solution layer closed to the surface of steel. Therefore, the corrosion rate of steel reached a significant high level due to the increase of dissolution rate of Fe^{2+} at anode along with the decrease of anodic polarizability in rebar corrosion.

Differing from the process of wetting, enough oxygen was supplied during the process of drying cycle. Thus, the reduced corrosion layer (Fe_3O_4) could be oxidized again by the oxygen, which was explained in Eq. (8):

$$4Fe_3O_4+O_2+6H_2O\rightarrow 12FeOOH \quad (8)$$

Based on the above analysis, the electromotive force of the steel corrosion in the D/W cycle was involved in a series of complex cathodic as well as anodic reactions therefore it was almost impossible to be accurately described. In this work, the steel was judged in critical corrosion state in the case of potential ranging from -0.400 to -0.516 V. Furthermore, the steel was in moderate corrosion

rate state when the potential ranged from -0.516 to -0.710 V and in high corrosion rate state when the potential was more negative than -0.710 V, as presented in Table 4.

Table 4. Half-cell potential of steel in different corrosion condition with respect to MnO_2 RE.

Corrosion state	Potential vs. embedded MnO_2 RE (V)
Passive state	> - 0.400
Critical corrosion state	- 0.400 to - 0.516
Moderate corrosion rate state	- 0.516 to - 0.710
High corrosion rate state	< - 0.710

Nevertheless, measurement of potential of embedded reference electrode in these previous researches was performed by means of the external electrodes[12,18,20,28] and concrete cover produced huge influences on the obtained results. More importantly, it was necessary to build the relationship between HCP of steel with respect to the embedded reference electrode and these different conditions determined according to the corrosion current density measured by other electrochemical techniques such as EIS and LP. In this investigation, estimation of steel condition could be realized through measurement of steel potential with respect to the embedded MnO_2 RE according to the built relationship between potential of steel and the correspond condition. Meanwhile, continuous monitoring of steel condition was conducted based on the accurate measurement of steel potential through embedded MnO_2 RE because HCP technique was a non-destructive technique and implement of this technique only needs the aid of a voltmeter.

3.4 Morphology observation

Fig. 12 indicates the surface morphologies of steel after exposure to drying/wetting (D/W) cycle 6 and 12, respectively. As shown in Fig. 12(a), no rust points can be observed on the steel surface even though the corrosion has been initiated.

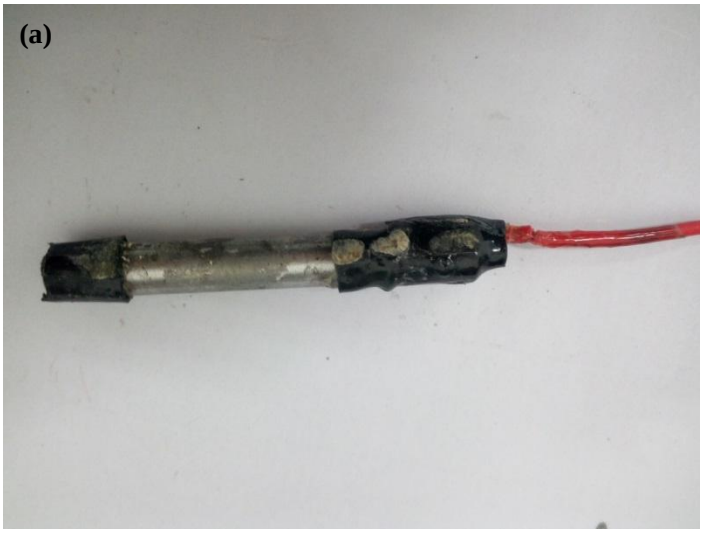

Figure 12. The surface morphologies of steel in concrete after different drying/wetting cycles. (a) cycle 6, and (b) cycle 12.

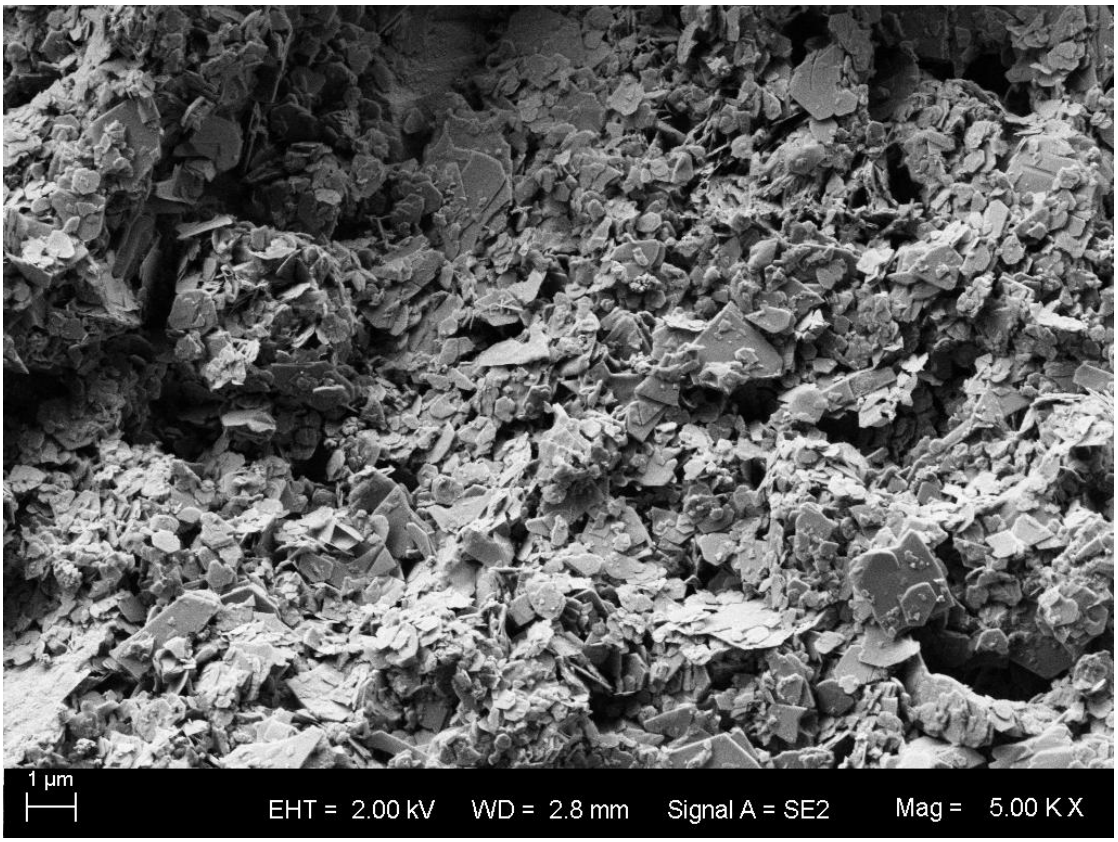

Figure 13. The micro-morphology of rust product of steel in concrete under drying/wetting exposure to chloride solution.

According to our previous literature[21], the accumulation rate of corrosion products was much slower compared to that of corrosion current density of steel. Besides, obvious dark brown rust area is detected on surface of steel after cycle 12 (presented in Fig. 12b) meanwhile rust products propagates

from the junction between the exposed steel surface and the sealing part to the central section of steel. Furthermore, micro-morphology of rust product of steel is shown in Fig. 13. It can be clearly found out that rust product consists of loose and irregular flaky substance whose dimension ranges from hundreds of nanometer to several micrometer. A large amount of pores are also observed on the surface of rust product. Based on the above analysis, the promotion effect of rust product on the resistance of protective film to corrosion is negligible.

4. CONCLUSIONS

Based on the results of the present investigation, following conclusions can be drawn:

(1) The polarization resistance of steel is derived from the slope of LP curve and obtained by adding the resistance of protective film to the charge transfer resistance determined from EIS data by means of the equilibrium circuit model. Then the corrosion current density of steel is calculated based on the obtained polarization resistance according to the Stern-Geary equation. Furthermore, ″divergent region″ must be introduced in the determination of corrosion condition of steel.

(2) The half-cell potential (HCP) of steel in concrete with respect to MnO_2 RE are higher than -0.400 V, -0.400 to -0.516 V, -0.516 to -0.710 V and lower than -0.710 V for passive condition, critical corrosion condition, moderate corrosion rate condition and high corrosion rate condition respectively.

(3) Continuous non-destructive monitoring the development of corrosion condition of steel in concrete is realized by the application of embedded reference electrode. Moreover, quick determination of corrosion information concerning the steel condition is achieved through the HCP technique.

ACKNOWLEDGEMENTS

The authors gratefully acknowledge the support provided by the National Key Technology Research and Development Program of the Ministry of Science and Technology of China (2015BAB07B04), the Fundamental Research Funds for the Central Universities (2016B04514, 2015B25814 and 2015B26714), the Graduate research and innovation projects in Jiangsu Province (KYZZ16_0276).

References

1. Z.Q. Jin, X. Zhao, T.J. Zhao and L. Yang, *Int. J. Electrochem. Sc.*, 11 (2016) 8779-8796.
2. S. Ahmad, *Cem. Concr. Compos.*, 25 (4) (2003) 459-471.
3. Z.H. Zou, J. Wu and Z. Wang, *Corrosion Engineering, Science and Technology*, 51 (8) (2016) 588-595.
4. B. Elsener, *Constr. Build. Mater.*, 15 (2) (2001) 133-139.
5. B. Elsener, C. Andrade, J. Gulikers, R. Polder and M. Raupach, *Mater. Struct.*, 36 (261) (2003) 461-471.
6. H. Song and V. Saraswathy, *Int. J. Electrochem. Sc.*, 2 (1) (2007) 1-28.
7. C. Ye, R. Hu, S. Dong, X. Zhang, R. Hou, R. Du, C. Lin and J. Pan, *J. Electroanal. Chem.*, 688 (2013) 275-281.
8. D.V. Ribeiro and J.C.C. Abrantes, *Constr. Build. Mater.*, 111 (2016) 98-104.

9. H.W. Feng, L.L. Cui and M. Zhang, *Int. J. Electrochem. Sc.*, (11) (2016) 4658-4666.
10. Y. Wang, Y. Zuo, X. Zhao and S. Zha, *Appl. Surf. Sci.*, 379 (2016) 98-110.
11. F. Shaheen and B. Pradhan, *Cem.Concr. Res.*, 91 (2017) 73-86.
12. M. Jin, J. Xu, L. Jiang, G. Gao, H. Chu, C. Xiong, H. Gao and P. Jiang, *Electrochemistry*, 82 (12) (2014) 1040-1046.
13. J. Wei, X.X. Fu, J.H. Dong and W. Ke, *J. Mater. Sci. Technol.*, 28 (10) (2012) 905-912.
14. G.S. Duffo and S.B. Farina, *Constr. Build. Mater.*, 23 (8) (2009) 2746-2751.
15. Y. Abbas, F. Pargar, W. Olthuis and A. van den Berg, *Procedia Engineering*, 87 (2014) 1437-1440.
16. W. He and R. He, *Int. J. Electrochem. Sc.*, 11 (2016) 7801-7810.
17. G.S. Duffó, S.B. Farina and C.M. Giordano, *Electrochim. Acta*, 54 (3) (2009) 1010-1020.
18. S. Muralidharan, V. Saraswathy, K. Thangavel and N. Palaniswamy, *Sensors and Actuators B: Chemical*, 130 (2) (2008) 864-870.
19. S. Muralidharan, V. Saraswathy, A. Madhavamayandi, K. Thangavel and N. Palaniswamy, *Electrochim. Acta*, 53 (24) (2008) 7248-7254.
20. S.P. Karthick, S. Muralidharan, V. Saraswathy and K. Thangavel, *Sens. Actuators B: Chem.,*, 192 (2014) 303-309.
21. M. Jin, L. Jiang, S. Bai, S. Jiang, C. Xiong and Z. Song, *Int. J. Electrochem. Sc.*, 11 (9) (2016) 7890-7908.
22. U. Angst, B. Elsener, C.K. Larsen and Ø. Vennesland, *Cem. Concr. Res.*, 39 (12) (2009) 1122-1138.
23. G. Qiao, B. Guo, Z. Li, J. Ou and Z. He, *Constr. Build. Mater.*, 134 (2017) 388-396.
24. J. Shi and J. Ming, *Constr. Build. Mater.*, 136 (2017) 118-125.
25. R.B. Polder and W.H.A. Peelen, *Cem. Concr. Compos*, 24 (5) (2002) 427-435.
26. D.A. Koleva, J.H.W. de Wit, K. van Breugel, Z.F. Lodhi and G. Ye, *J. Electrochem. Soc.*, 154 (5) (2007) C261-C271.
27. Y. Ji, M. Wu, Z. Tan, F. Gao and F. Liu, *Constr. Build. Mater.*, 73 (2014) 214-221.
28. M. Jin, L. Jiang, J. Xu, H. Chu, D. Tao, S. Bai and Y. Jia, *Electrochemistry*, 84 (6) (2016) 383-389.

© 2018 The Authors. Published by ESG (www.electrochemsci.org). This article is an open access article distributed under the terms and conditions of the Creative Commons Attribution license (http://creativecommons.org/licenses/by/4.0/).